Chemical Science

ROYAL SOCIETY OF CHEMISTRY

EDGE ARTICLE

View Article Online
View Journal | View Issue

Cite this: *Chem. Sci.*, 2023, **14**, 2745

All publication charges for this article have been paid for by the Royal Society of Chemistry

Received 2nd December 2022
Accepted 2nd January 2023

DOI: 10.1039/d2sc06620c

rsc.li/chemical-science

A "tug-of-war" effect tunes Li-ion transport and enhances the rate capability of lithium metal batteries†

Han Zhang,[ab] Ziqi Zeng,*[a] Mengchuang Liu,[a] Fenfen Ma,[c] Mingsheng Qin,[ab] Xinlan Wang,[ab] Yuanke Wu,[ab] Sheng Lei,[ab] Shijie Cheng[a] and Jia Xie *[a]

"Solvent-in-salt" electrolytes (high-concentration electrolytes (HCEs)) and diluted high-concentration electrolytes (DHCEs) show great promise for reviving secondary lithium metal batteries (LMBs). However, the inherently sluggish Li^+ transport of such electrolytes limits the high-rate capability of LMBs for practical conditions. Here, we discovered a "tug-of-war" effect in a multilayer solvation sheath that promoted the rate capability of LMBs; the pulling force of solvent–nonsolvent interactions competed with the compressive force of Li^+-nonsolvent interactions. By elaborately manipulating the pulling and compressive effects, the interaction between Li^+ and the solvent was weakened, leading to a loosened solvation sheath. Thereby, the developed electrolytes enabled a high Li^+ transference number (0.65) and a Li (50 μm)||NCM712 (4 mA h cm^{-2}) full cell exhibited long-term cycling stability (160 cycles; 80% capacity retention) at a high rate of 0.33C (1.32 mA cm^{-2}). Notably, Li (50 μm)||$LiFePO_4$ (LFP; 17.4 mg cm^{-2}) cells with a designed electrolyte reached a capacity retention of 80% after 1450 cycles at a rate of 0.66C. An 6 Ah Li||LFP pouch cell (over 250 W h kg^{-1}) showed excellent cycling stability (130 cycles, 96% capacity retention) under practical conditions. This design concept for an electrolyte provides a promising path to build high-energy-density and high-rate LMBs.

Introduction

Lithium metal batteries (LMBs) are considered as fruitful candidates for high-energy-density power source.[1–3] However, typically LMBs express inferior electrochemical performance due to the low coulombic efficiency (CE) of the lithium metal anode (LMA) in nonaqueous electrolytes, which induces continuous consumption of both electrolyte and LMA.[4–6] Among the various factors affecting the electrochemical performance of LMBs, the electrolyte plays a vital part in uncontrollable side reactions between the LMA and electrolytes.[7,8] By fine-tuning electrolyte formulations, the solid electrolyte interphase (SEI) chemistry and Li morphology can be regulated to improve the CE and cyclability of LMBs.[9,10] Electrolyte design has shown a great prospect for building better LMBs, including weakly solvating electrolytes (WSEs),[11] high-concentration electrolytes (HCEs),[12] and diluted high-concentration electrolytes (DHCEs).[13] Although these promising electrolytes provide high CE (>99%) and derive robust SEI and cathode electrolyte interphase (CEI) on both the LMA and cathode, the limited rate performance of LMBs cannot meet the demand for commercialization.[14–26] Specifically, ionic conductivity and the Li^+ transference number (T_{Li^+}; ionic current is carried predominantly by Li^+) are two critical parameters to measure the mobility of Li^+ in electrolytes. The low mobility of Li^+ will aggravate the concentration polarization in the electrolyte, thereby accelerating the formation of lithium dendrites. Therefore, high ionic conductivity and especially high T_{Li^+} are indispensable requirements in developing electrolytes for high-rate LMBs.[27–30]

For WSEs, rational tuning of molecule structures is an effective method to achieve high performance in LMBs.[31–33] However, a weak solvating solvent with insufficient solvation ability leads to low solubility towards salts, ultimately leading to a poor capability of Li^+ transport. As another highly competitive candidate, a DHCE expresses superiority in terms of viscosity compared with a HCE and shows great potential for practical application. Despite the sufficient solvation ability of the main solvent in a DHCE, the absence of free solvent and the tough constraining force between the Li^+-solvent in a strong solvation structure makes it difficult to support fast Li^+ transport ability.[34–38] Inspired from WSEs and DHCEs, it is critical to

[a]State Key Laboratory of Advanced Electromagnetic Engineering and Technology, School of Electrical and Electronic Engineering, Huazhong University of Science and Technology, Wuhan 430074, Hubei, China. E-mail: xiejia@hust.edu.cn; ziqizeng@hust.edu.cn

[b]State Key Laboratory of Materials Processing and Die & Mould Technology, School of Materials Science and Engineering, Huazhong University of Science and Technology, Wuhan 430074, Hubei, China

[c]GuSu Laboratory of Materials, Suzhou 215123, Jiangsu, China

† Electronic supplementary information (ESI) available. See DOI: https://doi.org/10.1039/d2sc06620c

achieve a balance between insufficient solvation and sufficient solvation in ideal electrolytes for fast Li^+ transport.[39–41] Thus, new strategies are required to innovate electrolyte design for maintaining the capability of solvating Li^+ but simultaneously weakening fetters on Li^+ of strong solvation structure. Considering the universality of non-coordinating solvents inevitably affect the interactions strength of Li^+-solvent through intermolecular force, manipulating non-coordinating solvents with diverse interaction capabilities may be an effective strategy to relieve the strong bonding of Li^+-solvents.[42,66] Up to now, a loosened solvation structure by fine-tuning of non-coordinating solvents are desirable yet not well studied to realize both reversible Li plating/stripping and fast Li^+ transfer.

In this work, we discovered a "tug-of-war" effect in multilayer solvation sheaths. That is, direct solvent–nonsolvent and indirect Li^+–nonsolvent interactions were leveraged to tune the binding energy between Li^+ and the main solvent. As a paradigm, a non-coordinating solvent (1,3,5-trifluorobenzene (F_3B)) was introduced into a fluorobenzene (FB)-based DHCE (denoted "DHCE2"), which delivered a high T_{Li^+} (0.65) without altering the primary solvation structure of Li^+ to achieve a CE up to 99.2% under 3 mA cm^{-1}. Notably, different abilities of intermolecular interaction between F_3B and FB to the solvent weakened the interaction between Li^+ and the main solvent, as evidenced by the spectroscopy (Raman, nuclear magnetic resonance (NMR), pulsed field gradient nuclear magnetic resonance (PFG-NMR)) and *ab initio* molecular dynamics (AIMD). Consequently, a loosened solvation sheath was achieved in DHCE2 for improving the kinetics of Li^+ transfer. A superb rate capability using DHCE2 was achieved in a LMB cell employing a Li-NCM712 cathode with an areal capacity of 2 mA h cm^{-2}. Moreover, a Li-NCM712 full cell was evaluated under practical conditions of high-NCM712 loading (4 mA h cm^{-2}) and thin Li (50 μm), which sustained 160 cycles with 80% capacity retention at a high rate (0.33C; 1.32 mA cm^{-2}) in DHCE2 while only 50 cycles were obtained in the control. Impressively, a Li (50 μm)–$LiFePO_4$ (LFP; 17.4 mg cm^{-2}) coin cell with a lean electrolyte (3 g A h^{-1}) using such an electrolyte achieved over 1450 cycles at a rate of 0.66 C. Meanwhile, the 6 Ah Li‖LFP pouch cell delivered energy density of over 250 W h kg^{-1} and outstanding lifespan under practical conditions (lean electrolyte: 3 g A h^{-1}; high areal capacity: 3.4 mA h cm^{-2}; limited Li: 50 μm; high discharge current: 1.2 A). Overall, we demonstrated a tug-of-war effect that could be utilized to facilitate Li^+ transport in a DHCE, shedding a new direction for building high-rate LMBs under practical conditions.

Results and discussion

The critical aim in this work was to improve rate capability of well-performing DHCE electrolytes. Despite high stability towards Li metal anodes, hydrofluoroether-based DHCE has the drawbacks of insufficient kinetics. Previously, we showed that F_3B could assist a FB-based DHCE in obviously boosting thermodynamic and interfacial stabilities,[43] but also significantly enhanced the high-rate capability compared with other DHCEs, yet the mechanism of improved kinetics was not investigated systematically. Therefore, F_3B was introduced tentatively into a FB-based DHCE with an increased dosage gradient, denoted as DHCE1, DHCE2, and DHCE5 (DHCE: 1.87 g of LiFSI was dissolved in 1.5 ml of DME and 3 ml of FB; DHCE1: 1.87 g of LiFSI was dissolved in 1.5 ml of DME, 2.9 ml of FB, and 0.1 ml of F_3B; DHCE2: 1.87 g of LiFSI was dissolved in 1.5 ml of DME, 2.8 ml of FB, and 0.2 ml of F_3B; DHCE5: 1.87 g of LiFSI was dissolved in 1.5 ml of DME, 2.5 ml of FB, and 0.5 ml of F_3B) to achieve in-depth understanding of the functions of F_3B non-coordinating solvents for high-rate DHCE applications. The ionic conductivity (a key indicator for the diffusion of ions in bulk electrolytes) was first measured at room temperature (Fig. 1a and Table S1†). Different DHCEs delivered an almost identical ionic conductivity, demonstrating that F_3B as the additive barely affected the ionic conductivity of DHCEs. Moreover, the T_{Li^+} of various electrolytes is shown in Fig. 1b and Figure S1.† As the amount of F_3B increased, the T_{Li^+} first rose and then declined. Noticeably, DHCE2 delivered the highest T_{Li^+} up to 0.65, indicating the fastest transport ability of Li^+. Based on calculations (Fig. 1c), the Li^+ conductivity in DHCE2 was higher than FSI^- conductivity, suggesting a superb Li^+ transfer capability. To better evaluate the effect of Li^+ migration on electrochemical performance, the rate performance of Li-NCM712 was measured (Fig. 1d). DHCE2 showed significantly improved rate capability in the Li-NCM712 cell compared with that of other DHCEs, demonstrating superior Li^+ diffusion kinetics, which is promising for the construction of high-energy-density and high-power-density LMBs. Beyond use of a potentiostatic polarization method to measure T_{Li^+}, PFG-NMR spectroscopy was also employed to examine Li^+ transference number ($T_{Li^+}^{NMR}$). As shown in Fig. 1e, the lithium transference number ($T_{Li^+} = D_{Li^+}/(D_{Li^+} + D_{FSI^-})$) was much higher in DHCE2 compared with that in other DHCEs. The transference number plays a critical part in determining the morphology and cycling stability of lithium.[44,45] The Sand's capacity using the model proposed by Bai was also calculated using the following equation,[46]

$$C_{Sand} = Jt_{Sand} = \frac{\pi D_{app}(Z_c C_0 F)^2}{4J(1-t_+)^2}$$

where J is the current density, D_{app} is the diffusion coefficient, Z_c is the charge number of the cation, C_0 is the bulk concentration, F is the Faraday constant, and t_+ is the cation transference number. Fig. 1f shows the Sand's capacity of DHCE and DHCE2 with respect to the current density. In this case, DHCE2 showed the highest Sand's capacity. This finding implied that cells with DHCE2 were less prone to ion depletion, which is one of the main driving forces for uncontrollable dendrite growth. This work points to a new direction to promote Li^+ migration in a DHCE, which has been rarely explored. To understand the role of F_3B in enhancing Li^+ transfer in a DHCE, a series of DHCEs with an increased F_3B gradient were used to analyse the solvation structure of FSI^- by Raman vibrational spectroscopy (Fig. 2a). The heterogeneous ion-rich domain networks at 720–780 cm^{-1} were defined as a contact ion pair (CIP), small

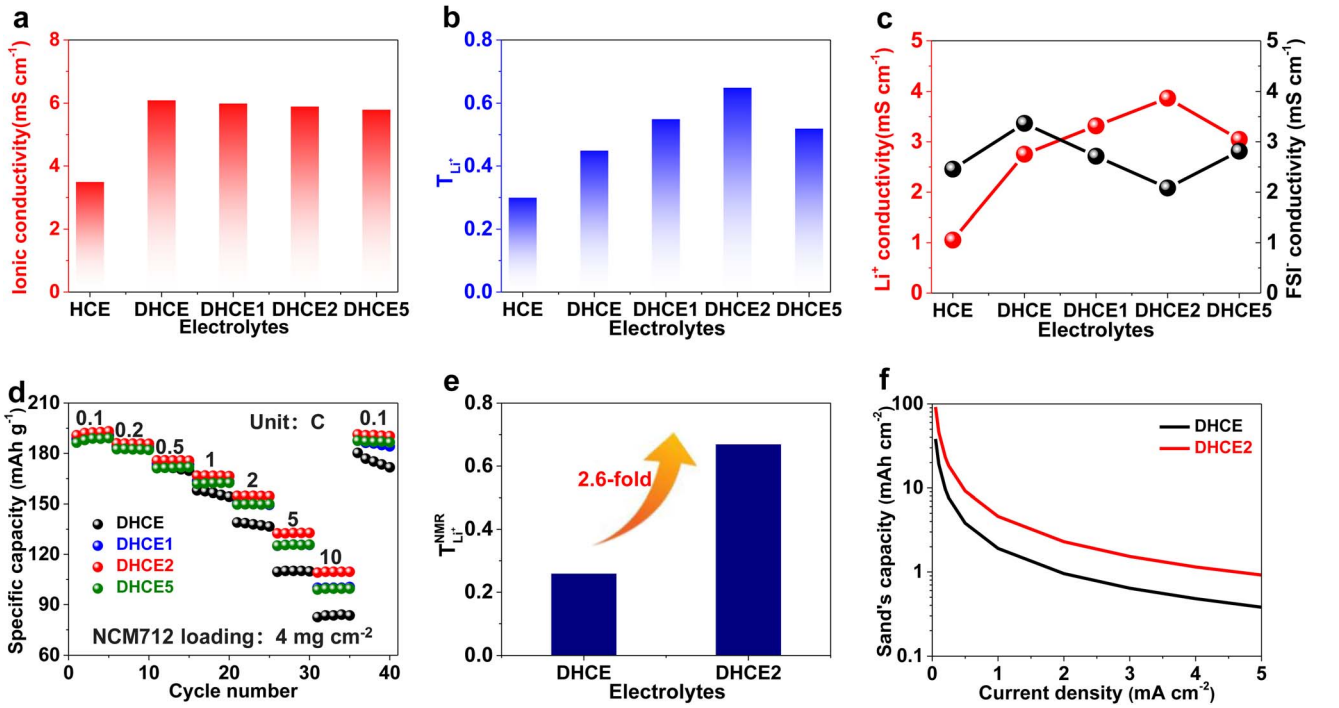

Fig. 1 (a) Ionic conductivity of different electrolytes. (b) Li^+ transference number of different electrolytes. (c) Li^+ and FSI^- conductivity of different electrolytes. (d) Rate performance of Li-NCM712 cells in different electrolytes. (e) Li^+ transference number obtained through pulsed field gradient NMR spectroscopy for different electrolytes. (f) Sand's capacity of different electrolytes *versus* current density.

aggregate (AGG), and nanometric aggregate (n-AGG), suggesting that the addition of F_3B to DHCE barely affected the Li^+ primary solvation sheath (Li^+-FSI^--DME). Interestingly, F_3B with a lower dielectric constant ($\varepsilon = 2$)[47] was likely to favour the formation of n-AGG. With an increase in F_3B content in a DHCE, the peak area ratio assigned to n-AGG increased to 14.3% in DHCE2. According to previous research,[48] ion migration in n-AGG is correlated to "hopping" conduction and may have a positive effect on improving Li^+ transport. Besides, n-AGG may lead to the formation of an anion-derived SEI. Notably, with excess F_3B in DHCE5, the signal of n-AGG disappeared. Despite DHCE5 sharing the same solvation structure with DHCE, the T_{Li^+} was higher than that of DHCE (Fig. 1b). Therefore, we speculated that the function of F_3B was more than driving the formation of n-AGG. Other intermolecular forces (*e.g.*, solvent–solvent interaction) probably influenced the Li^+ transfer.

Furthermore, NMR spectroscopy was applied to study the elaborate solvation environment around the Li^+ and solvent–solvent interactions (Fig. 3a). From DHCE to DHCE1 and DHCE2, ^7Li signal showed an obvious downfield shift, indicating a deshielding effect around Li^+ and perhaps formation of a loosened solvation sheath, leading to improved Li^+ transfer kinetics. Notably, the broadened signal of Li^+ in DHCE2 suggested a disorder in the local environment of Li^+, as evidenced by n-AGG formation. However, DHCE5 showed a shielding effect around Li^+ compared with DHCE2, but expressed a deshielding effect compared with DHCE, possibly verifying a moderately loosened solvation sheath. As shown in Fig. 3b, the ^1H NMR chemical shift revealed an opposite change towards ^7Li NMR, demonstrating that the interaction between Li^+-DME was first weakened and then strengthened with an increase in F_3B. Correspondingly, the interactions between Li^+ and FSI^- were first enhanced and then weakened, as evidenced by ^{19}F NMR spectroscopy (Fig. 3c). As shown in Fig. S2,† the ^{19}F NMR spectra of FB and F_3B in these DHCE systems were highly consistent with the above analysis. These results demonstrated that the non-coordinating F_3B was essential for regulating the strong interaction of Li^+-FSI^--DME. To further confirm this speculation, the ^1H chemical shifts of FB, F_3B and DME mixtures were acquired to demonstrate intermolecular interactions. Fig. S3a and b† suggest the existence of molecular interactions between FB and F_3B, FB and DME, as well as F_3B and DME. Even with mixing of all three solvents (FB, F_3B and DME), the molecular interaction was not counteracted. After solvation of the Li salt, ^1H NMR spectroscopy showed an identical variation tendency (Fig. S3c and d†), which suggested that the solvent–solvent interactions were preserved despite the presence of cations. To describe the relative strength of intermolecular forces qualitatively, identical amounts of FB and F_3B were added to DME and then ^1H NMR spectroscopy was done (Fig. 3d). The peaks of DME had a higher field shift after adding FB compared with F_3B, which directly indicated a stronger molecular interaction between DME and FB than that between DME and F_3B. The results from NMR spectroscopy corresponded closely to our conjecture that different interaction abilities between F_3B and FB could loosen the Li^+-FSI^--DME solvation structure.

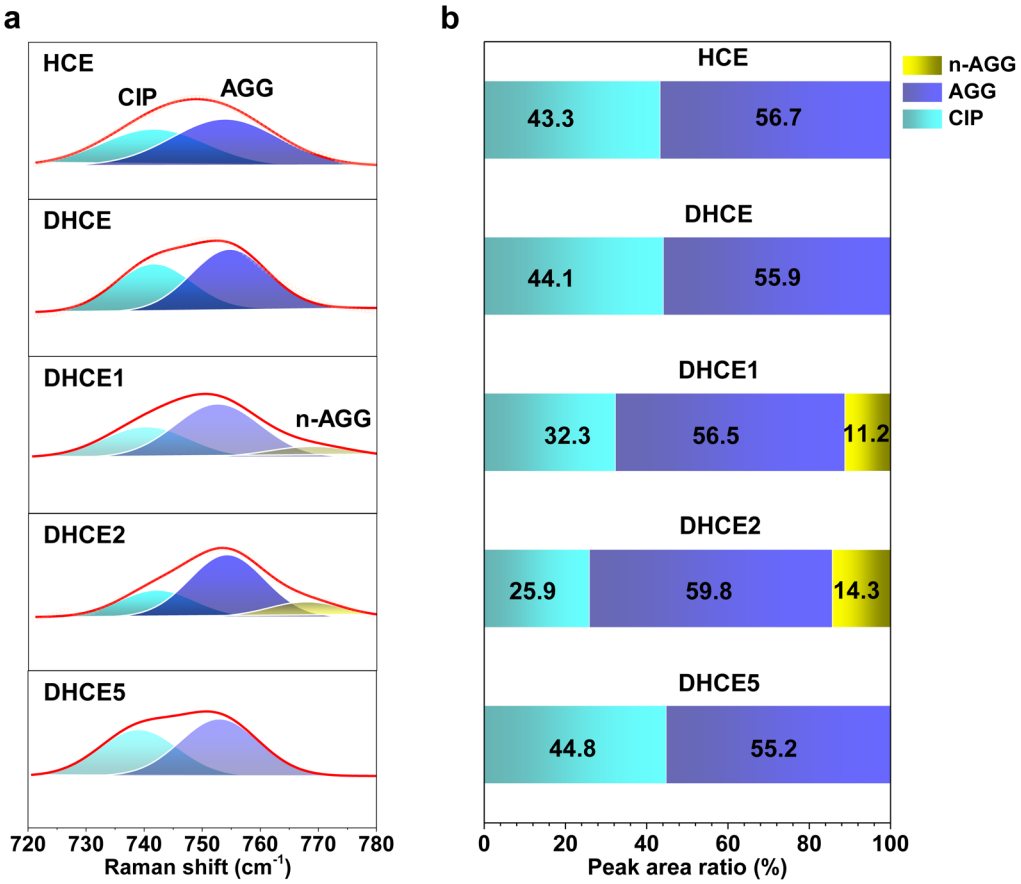

Fig. 2 (a) Raman spectra of FSI^- in various aggregate clusters. (b) Peak area ratio of CIP, AGG, and n-AGG in HCE, DHCE, DHCE1, DHCE2, and DHCE5 obtained from the fitting results of Raman spectra.

To further confirm the effect of F_3B additives, DHCE and DHCE2 were described using AIMD simulations. Snapshots of simulated electrolytes are shown in Fig. 4a–f. The AIMD trajectory was used to obtain the radial distribution functions of Li–O_{DME} and Li–O_{FSI^-} and F(FB/F_3B)–H(DME) pairs. A sharp peak at 1.92 Å was associated with the Li–O_{DME} pairs for the DHCE systems. In comparison, a weaker peak prolonged to 1.96 Å in the DHCE2 system (Fig. 4g), suggesting that Li^+ was loosely coordinated with DME. Meanwhile, a mild peak at 2.15 Å was attributed to the Li–O_{FSI^-} pairs for the DHCE, shifting to 1.95 Å in DHCE2 (Fig. 4h).

This result indicated that interactions between Li^+ and FSI^- were slightly strengthened in DHCE2 through weakening the interactions between Li^+ and DME, which was consistent with the result of ^{19}F NMR spectroscopy. Moreover, the RDF of F(FB/F_3B)–H(DME) pairs in Fig. 4i revealed that, within a radius of 5 Å, FB was predominant, This result confirmed that FB may be close to the primary solvation structure, whereas F_3B is away from the primary solvation structure with high probability, which further supports the idea of a stronger molecular interaction between DME and FB than that between DME and F_3B. The different locations of FB and F_3B outside the primary solvation sheath seem to be the main reason for promoting Li^+ transport capability. Hence, we propose a possible multilayer solvation sheath model. Based on the probability of the diluent appearing at different locations outside the primary solvation structure, the diluent in DHCE is simplified as two layers: inner layer (close to the primary solvation structure) and outer layer (away from the primary solvation structure). This hypothesis is similar to theories in previous reports on the formation of multilayer solvation sheaths in a DHCE using non-coordinating solvents.[49] The inner layer of FB is likely to interact with DME through intermolecular forces, which was demonstrated in our recent report,[42] showing that FB "pulls" DME (denoted as "strong drag effect"). The outer layer of FB probably is attracted to Li^+ according to classical Coulomb force theory due to the electron-rich π-conjugated system of FB showing a strong compressive effect on the primary solvation sheath, which is also consistent with our previous result.[17] It has been suggested that FB has different effects on the primary solvation structure depending on its location. The pristine DHCE possesses a strong solvation sheath and sluggish Li^+ transfer, suggesting that the compressive effect exceeds the drag effect towards Li^+-FSI^--DME. In DHCE1 and DHCE2, owing to the reduced density of the electron cloud of the benzene ring and lower dielectric constant arising from the polyfluoride substitution, F_3B likely appears at the outer layer to replace FB and expresses a weakened compressive effect compared with FB, while the inner

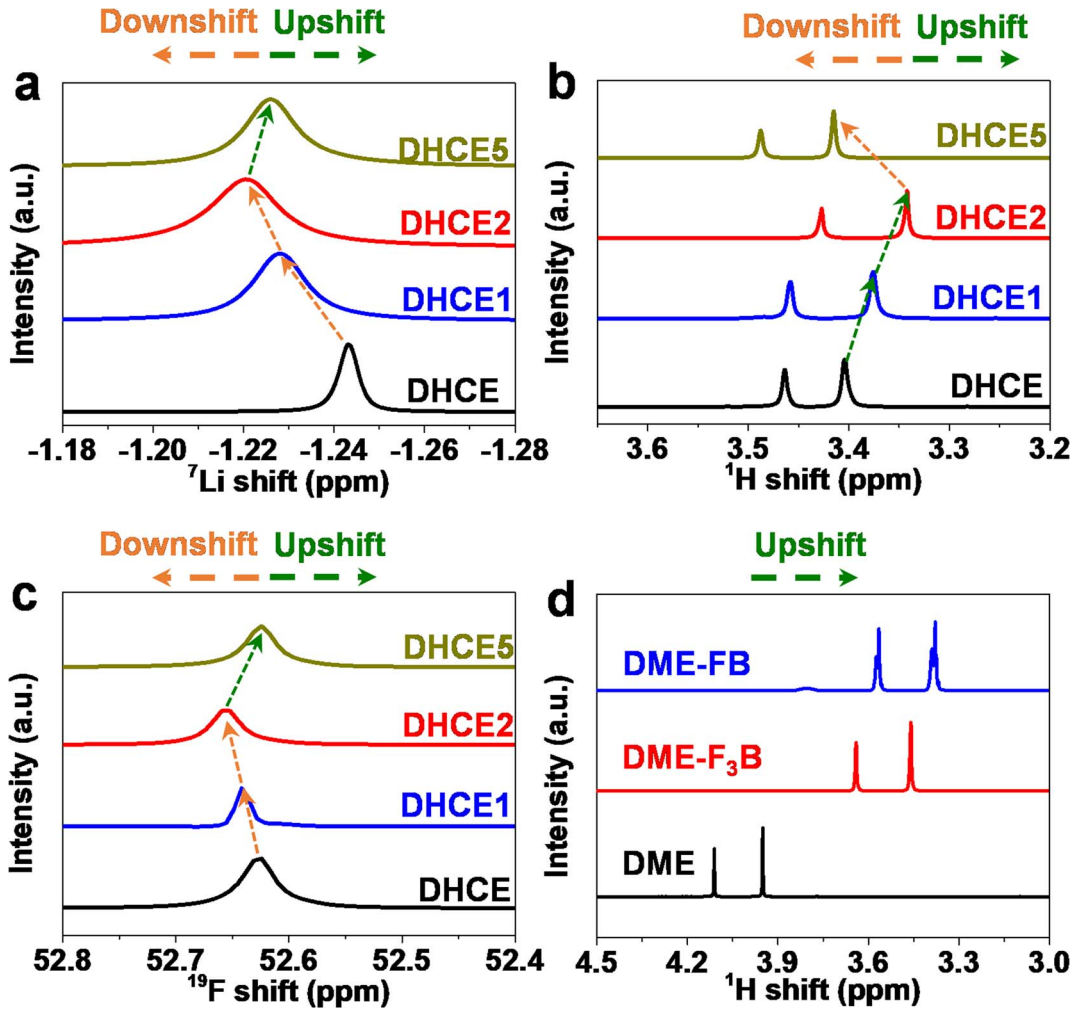

Fig. 3 (a) ^{7}Li NMR spectroscopy, (b) ^{1}H NMR spectroscopy, and (c) FSI^{-} in ^{19}F NMR spectroscopy of different electrolytes. (d) ^{1}H NMR spectroscopy of a mixture of different solvents.

layer of FB with a strong drag effect remains. The compressive effect was outperformed by the drag effect towards Li^{+}-FSI^{-}-DME in DHCE1 and DHCE2, leading to a loosened solvation sheath and fast Li^{+} transfer. Further increase in F_3B (DHCE5) led to excess F_3B beginning to reach the inner layer, weakening the drag effect, thus leading to a moderately loosened solvation sheath and relatively fast Li^{+} transfer. In short, non-coordinating solvents with diverse interactions were manipulated to alter the constraints on Li^{+} and accelerate its transport kinetics. A summary of current understanding on the intermolecular force of F_3B on Li^{+}-FSI^{-}-DME (based on a solvation unit) is illustrated schematically in Fig. 4j.

Linear sweep voltammetry (LSV) was conducted to determine the reduction and oxidation potentials of HCE, DHCE and DHCE2 (Fig. S4a and b†). In addition to LiFSI, the reduction potential of F_3B was higher than that of FB and DME. As shown in Fig. S4c,† the calculated LUMO level of F_3B was −1.03 eV, which was significantly lower than that of FB (−0.83 eV) and DME (0.22 eV), further demonstrating the facile reduction of F_3B rather than FB and DME on the surface of Li metal to form a LiF-rich protective layer. Benefiting from the lower HOMO level in F_3B (−7.64 eV) compared with FB (−7.08 eV) and DME (−7.18 eV), DHCE2 showed better anti-oxidation. These results indicate that DHCE2 possibly enabled compatibility with the LMA and high-voltage cathode materials. Li plating/stripping reversibility is crucial for realistic LMBs, and can be reflected by Li/Cu half cells. A comparison of the CE during long-term cycling at 0.5 mA cm^{-2} and 0.5 mA h cm^{-2} is shown in Fig. S5a–d.† Remarkably, a superior average CE of 99.4% was achieved over 800 cycles in DHCE2. Under the test condition of 3 mA cm^{-2} and 1 mA h cm^{-2}, the Li–Cu half-cell using DHCE showed an average CE of 98.8% and held steady for 200 cycles, followed by a sharp drop. In DHCE2, the CE could be further promoted to 99.2% and remained stable for over 250 cycles (Figs. 5a, S5e and f†). Hence, DHCE2 showed an excellent compatibility and high-rate capability with the Li metal anode. Furthermore, the cycling performance of a Li-NCM712 (4 mg cm^{-2}) coin cell with different electrolytes at 1 C is shown in Fig. 5b. The cycle life could be further correlated with the average voltage gap between charge and discharge

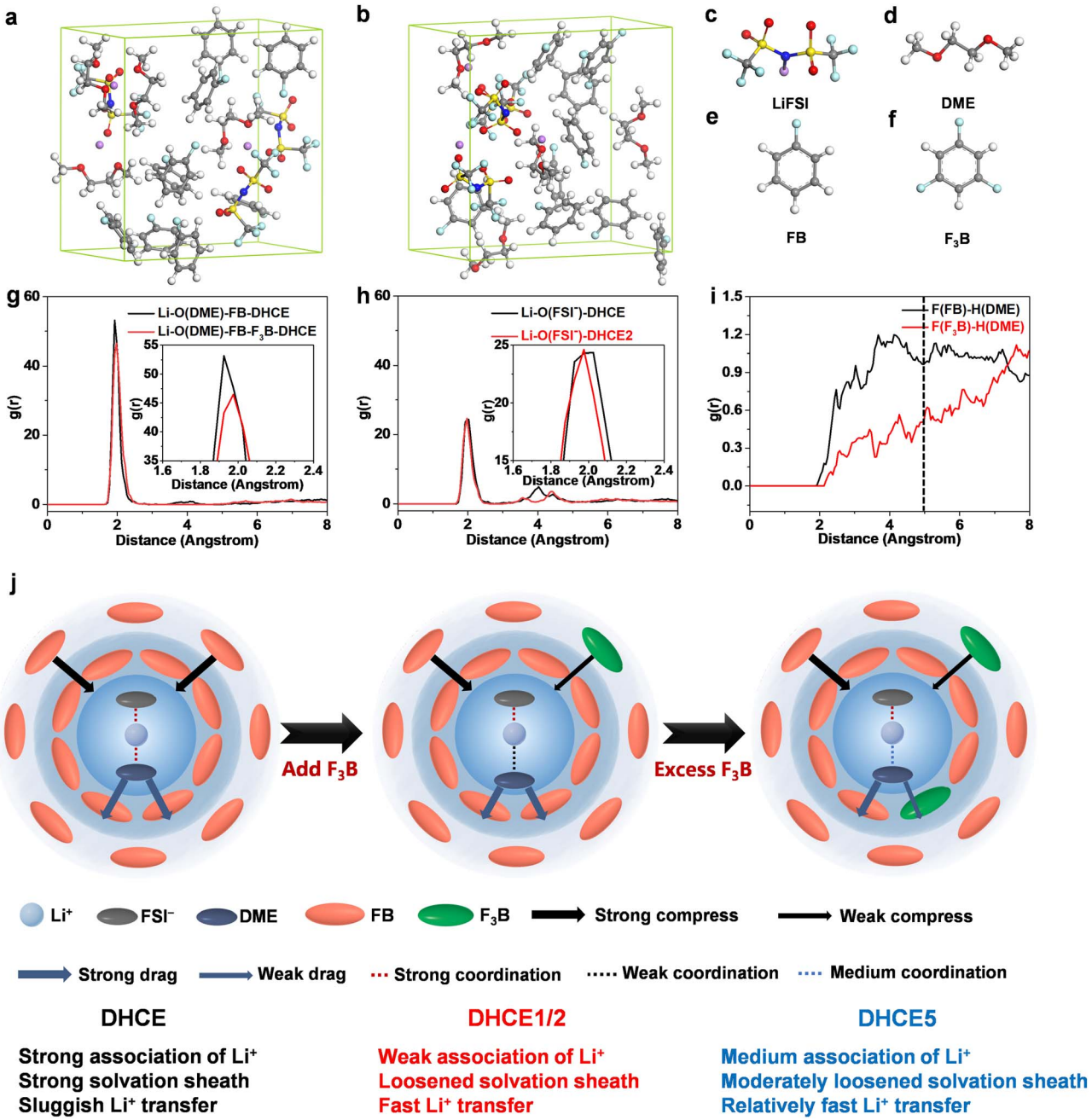

Fig. 4 AIMD simulation snapshots of selected electrolytes at 300 K: (a) DHCE, (b) DHCE2, and (c–f) ball-and-stick model. (g–i) Radial distribution functions of Li–O(DME), Li–O(FSI^-), and F(FB/F_3B)–H(DME) pairs calculated from AIMD trajectories at 300 K of DHCE and DHCE2. (j) Solvation sheath model in DHCE, DHCE1/2, and DHCE5 (schematic).

(Fig. S6†). After the formation cycles, Li-NCM712 with DHCE2 displayed stable cycling over 500 cycles (80% retention) and low overpotentials, while the control shows rapid capacity decay with sharply increased polarization. In addition, Li-NCM712 battery with medium loading (2 mA h cm^{-2}) is examined (Figs. 5c and S7†). The cell with DHCE exhibited continuous capacity decay. In contrast, an improved cyclability with more than a tripled lifetime was obtained by using DHCE2 (300 cycles, 80% retention). Moreover, the rate performance of Li-NCM712 (2 mA h cm^{-2}) in different electrolytes was evaluated (Figs. 5d and S8†). Using DHCE2, the cell delivered specific discharge capacities of 191, 183, 172, 158, 138, 123 and 111 mA h g^{-1} at 0.1, 0.2, 0.5, 1, 2, 3 and 4C, respectively. Impressively, under a high rate (4C), the specific discharge capacity of Li-NCM712 in DHCE2 was doubled compared with that of DHCE (58 mA h g^{-1}). Therefore, the developed electrolytes exhibited a prominent high-rate capability even at high mass loading, which holds great promise for practical application. The activation energy (E_a) was studied *via* temperature-dependent EIS ranging from −10 °C to 20 °C (Fig. S9†). The E_a was evaluated from the slopes of Arrhenius plots with the Arrhenius equation, $R^{-1} = A\exp(-E_a/RT)$, where A denotes the

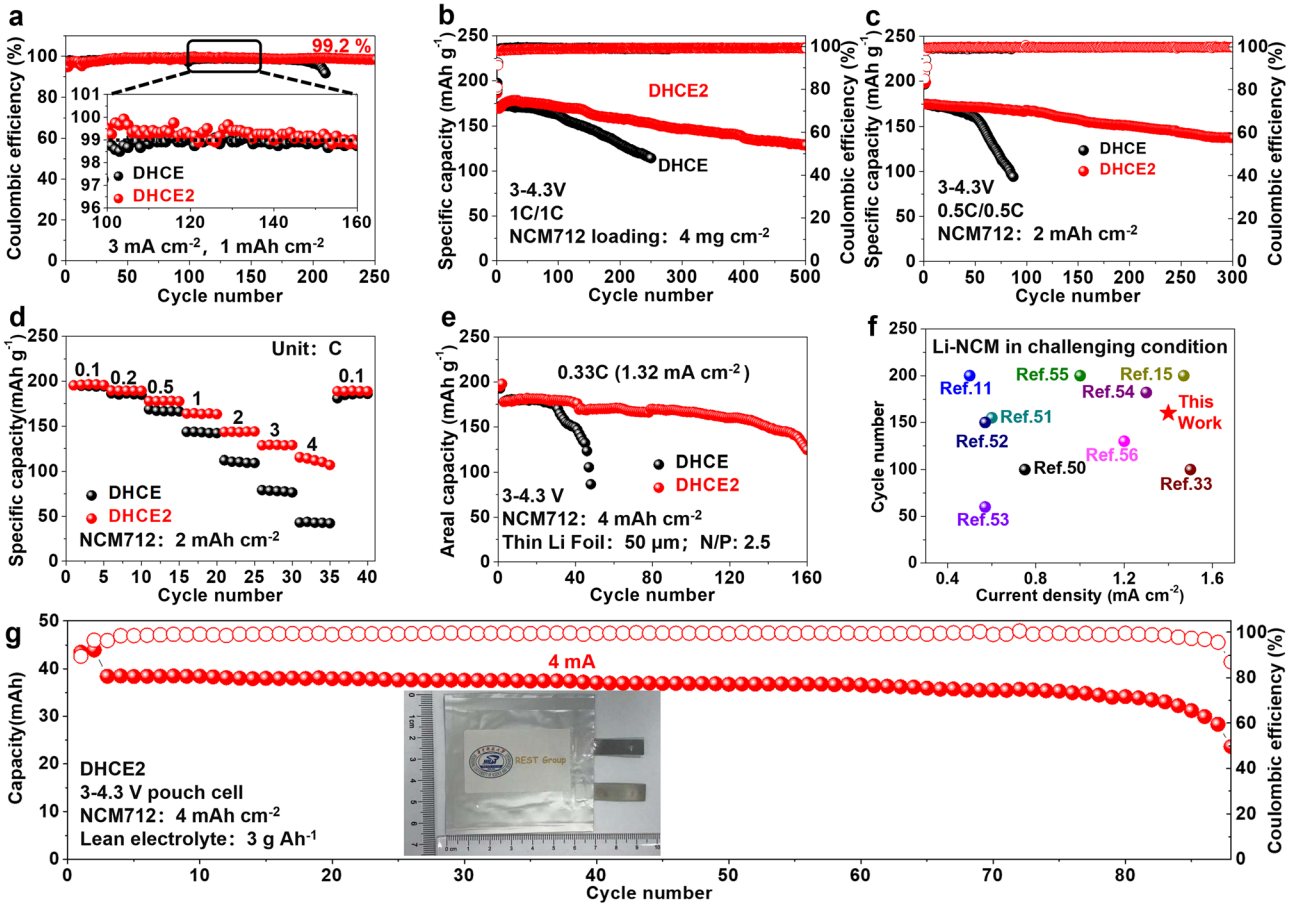

Fig. 5 (a) Li–Cu tests toward different electrolytes. Long-term cycling performance of Li-NCM712 cells. (b) NCM712 loading: 4 mg cm^{-2}. (c) Rate performance and (d) cycling performance of Li-NCM712 cells under different electrolytes (Li-NCM712: 3–4.3 V; areal capacity: 2 mA h cm^{-2}). (e) Cycling performance of a Li-NCM712 coin cell under challenging conditions (NCM712: 4 mA h cm^{-2}, 3–4.3 V, 50 μm Li). (f) Comparison of the electrochemical performance of Li-NCM cells in practical conditions. (g) Long-term cycling performance of a Li-NCM712 pouch cell (NCM712: 4 mA h cm^{-2}, 3–4.3 V, 200 μm Li, 3 g A h^{-1} electrolyte).

frequency factor, R is the ideal gas constant and T denotes the absolute temperature. The E_a for Li/Li symmetric cells in DHCE2 was calculated to be 15.2 kJ mol^{-1}, which was less than that of FB-DHCE (20.5 kJ mol^{-1}), thereby demonstrating kinetics improvement after adding F_3B. Also, an Li-NCM712 battery with ultra-high areal capacity (4 mA h cm^{-2}) was used to measure the rate performance. The cell with DHCE2 displayed a great rate capability, thanks to improved Li^+ transport kinetics, which far exceeded those of the reference electrolytes DHCE (Figs. S10 and S11†). Moreover, an Li-NCM712 battery with ultra-high areal capacity (4 mA h cm^{-2}) and limited Li (50 μm) was assembled. Figs. 5e and S12† show that the Li-NCM cell with DHCE2 maintained 70% capacity retention after 160 cycles at a high rate (0.33C; 1.32 mA cm^{-2}). The cell with FB-DHCE obtained 70% capacity retention after 60 cycles. To test the practicability of developed electrolytes in high-voltage LMBs, an Li-NCM712 full cell was built with an ultra-high areal capacity (4 mA h cm^{-2}), low N/P ratio (2.3) and low E/S ratio (3 g A h^{-1}). As shown in Figs. S13† and S14,† the battery using DHCE exhibited unstable cycling and rapid fading. In contrast, the cycling stability was improved significantly in DHCE2, where 70% capacity was retained after 110 cycles. Compared with other reports of advanced electrolytes in NCM-based LMBs under challenging conditions,[11,15,33,50–56] DHCE2 showed an unprecedented cycling performance at a high rate (Fig. 5f). Li-NCM712 pouch cells with DHCE2 were also constructed to verify the results under challenging conditions (NCM712: 4 mA h cm^{-2}, 200 μm Li, and 3 g A h^{-1} electrolyte). Such pouch cells delivered an outstanding capacity retention of 80% over 88 cycles (Figs. 5g, S15† and Table S2†). To pursue better electrochemical performance, we reduced the "free" DME molecules to the conventional DHCE concentration (LiFSI : DME : diluter = 1 : 1.2 : 3 by mol) for the study. First, we applied FB-DCHE (LiFSI : DME : FB = 1 : 1.2 : 3 by mol) and FB-F_3B-DHCE (LiFSI : DME : FB : F_3B = 1 : 1.2 : 2.8 : 0.2 by mol) to evaluate the effect of F_3B. To assess the durable interphase stability and high-rate performance of DHCE, LMBs with LFP cathodes were measured. A superior rate performance of the Li-LFP cell could be achieved in FB-F_3B-DHCE (Fig. 6a). Beyond low mass loading, the Li metal anode was also coupled with commercial LFP (17.4 mg cm^{-2}) to evaluate the rate performance, and further verification of kinetics enhancement by

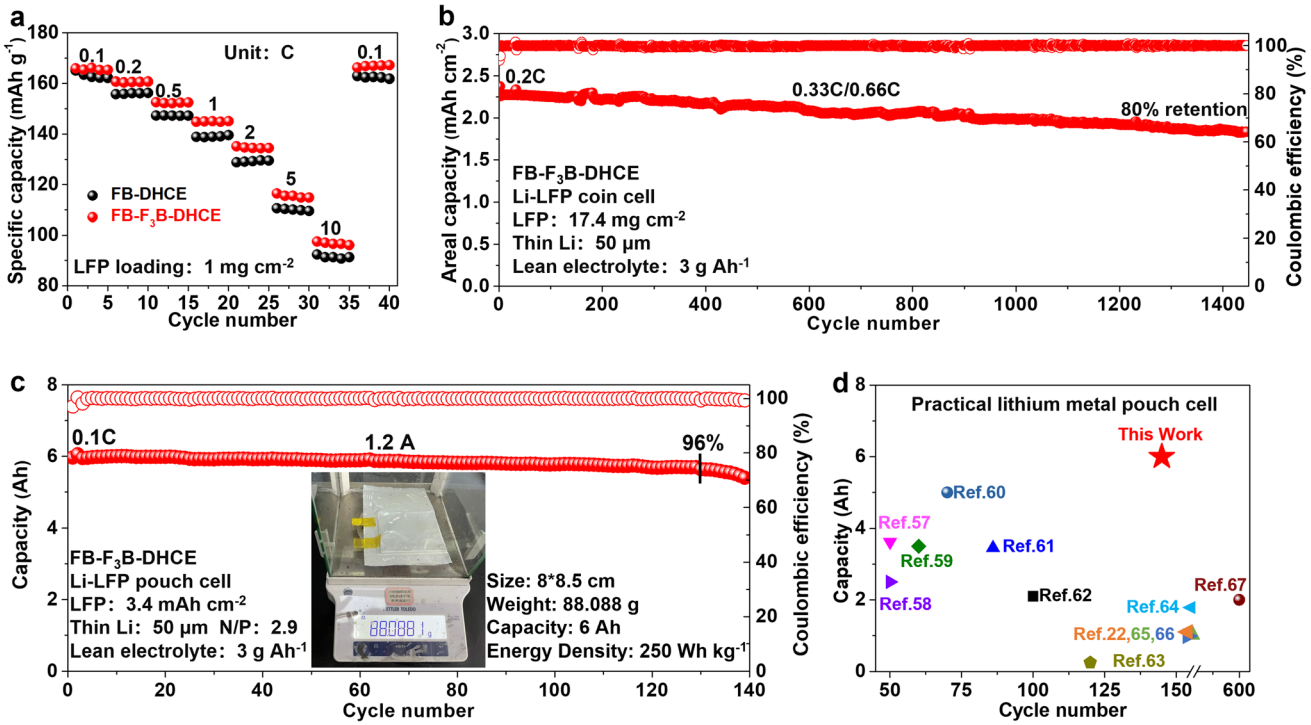

Fig. 6 (a) Rate performance towards FB-DHCE and FB-F_3B-DHCE. (b) Cycling performance of Li-LFP coin cells in FB-F_3B-DHCE (LFP loading: 17.4 mg cm^{-2}; thin Li: 50 μm; lean electrolyte: 3 g A h^{-1}). (c) Cycling performance of a 6-Ah-grade lithium metal pouch cell under realistic conditions in FB-F_3B-DHCE (insert: optical photo of the pouch cell with mass parameter). (d) Comparison of battery performance with other reported practical lithium metal pouch cells.

adding F_3B (Figs. S16 and S17†). As shown in Figs. 6b and S18,† excellent cycling performance (80% capacity after 1450 cycles) was realized in FB-F_3B-DHCE with high cathode loading (17.4 mg cm^{-2}), thin Li (50 μm), lean electrolyte (3 g A h^{-1}) and high rate (0.33C charging/0.66C discharging). This is the first time that LMBs have achieved such prolonged cycling performances in stringent conditions. Furthermore, a high-capacity lithium metal pouch cell was constructed to verify its potential practicality (Figs. 6c and S19†). A 15-layer (8 × 8.5 cm) Li||LFP pouch cell was assembled and measured under practical conditions: LFP areal capacity of 3.4 mA h cm^{-2}, E/C ratio of 3 g A h^{-1}, and a thin lithium foil of thickness 50 μm (N/P ratio of 2.9). The cell parameters are given in Fig. 6c. This Li||LFP pouch cell offered a cell-level specific energy of 250 W h kg^{-1} with a capacity of 6 A h at 0.2C (1.2 A). Long-term cycling of 130 cycles with 96% capacity retention was achieved using FB-F_3B-DHCE. The overall performance was one of the best among recently reported Ah-level practical lithium metal pouch cells (Fig. 6d).[22,57–67]

Conclusions

A unique tug-of-war effect was disclosed, which allowed manipulation of the pulling and compressive force in a multi-layer solvation sheath, achieving a loosened solvation sheath, and affording high-rate LMB. This effect was evidenced by spectroscopy (Raman, NMR, PFG-NMR) and AIMD, thereby revealing the underlying mechanisms of improved Li^+ transfer kinetics. Consequently, Li-NMC712 full batteries under a challenging condition (NCM712: 4 mA h cm^{-2}; Li: 50 μm; high current density: 1.32 mA cm^{-2}) showed stable cycling over 160 times. An Li-LFP coin cell under harsh conditions delivered a prominent cycling performance (1450 cycles; 80% retention) at a high discharge rate of 0.66C. A practical 6-Ah-grade Li-LFP pouch cell with a specific energy of 250 W h kg^{-1} delivered 130 cycles with a capacity retention of 96%. This work opens a new direction for using intermolecular force to improve Li^+ transport to develop novel DHCEs with high-rate capability for high-performance LMBs.

Data availability

All the data supporting this study are included in the manuscript and the ESI.†

Author contributions

J. Xie and Z. Zeng proposed the concept. H. Zhang prepared the materials, collected relevant data, and wrote the manuscript. All authors participated in data analyses and manuscript discussion.

Conflicts of interest

The authors declare no competing financial interests.

Acknowledgements

This work was supported financially by the National Key Research and Development Program of China (2022YFB2404800) and the National Natural Science Foundation of China (22008082, 21975087). The authors gratefully acknowledge the Analytical and Testing Center of HUST for allowing us to use its facilities. The authors thank the Shiyanjia Research Team (**https://www.shiyanjia.com/**) for help with NMR spectroscopy.

Notes and references

1 J. Liu, Z. Bao, Y. Cui, E. J. Dufek, J. B. Goodenough, P. Khalifah, Q. Li, B. Y. Liaw, P. Liu, A. Manthiram, Y. S. Meng, V. R. Subramanian, M. F. Toney, V. V. Viswanathan, M. S. Whittingham, J. Xiao, W. Xu, J. Yang, X.-Q. Yang and J.-G. Zhang, *Nat. Energy*, 2019, **4**, 180–186.

2 F. Duffner, N. Kronemeyer, J. Tübke, J. Leker, M. Winter and R. Schmuch, *Nat. Energy*, 2021, **6**, 123–134.

3 Y. Cao, M. Li, J. Lu, J. Liu and K. Amine, *Nat. Nanotechnol.*, 2019, **14**, 200–207.

4 S. Cao, X. He, L. Nie, J. Hu, M. Chen, Y. Han, K. Wang, K. Jiang and M. Zhou, *Adv. Sci.*, 2022, **9**, 2201147.

5 M.-Y. Zhou, X.-Q. Ding, J.-F. Ding, L.-P. Hou, P. Shi, J. Xie, B.-Q. Li, J.-Q. Huang, X.-Q. Zhang and Q. Zhang, *Joule*, 2022, **6**, 2122–2137.

6 C. Fang, J. Li, M. Zhang, Y. Zhang, F. Yang, J. Z. Lee, M.-H. Lee, J. Alvarado, M. A. Schroeder, Y. Yang, B. Lu, N. Williams, M. Ceja, L. Yang, M. Cai, J. Gu, K. Xu, X. Wang and Y. S. Meng, *Nature*, 2019, **572**, 511–515.

7 H. Wang, Z. Yu, X. Kong, W. Huang, Z. Zhang, D. G. Mackanic, X. Huang, J. Qin, Z. Bao and Y. Cui, *Adv. Mater.*, 2021, **33**, 2008619.

8 Y.-X. Zhan, P. Shi, C.-B. Jin, Y. Xiao, M.-Y. Zhou, C.-X. Bi, B.-Q. Li, X.-Q. Zhang and J.-Q. Huang, *Adv. Funct. Mater.*, 2022, **32**, 2206834.

9 A. J. Louli, A. Eldesoky, R. Weber, M. Genovese, M. Coon, J. deGooyer, Z. Deng, R. T. White, J. Lee, T. Rodgers, R. Petibon, S. Hy, S. J. H. Cheng and J. R. Dahn, *Nat. Energy*, 2020, **5**, 693–702.

10 C. V. Amanchukwu, Z. Yu, X. Kong, J. Qin, Y. Cui and Z. Bao, *J. Am. Chem. Soc.*, 2020, **142**, 7393–7403.

11 Z. Yu, H. Wang, X. Kong, W. Huang, Y. Tsao, D. G. Mackanic, K. Wang, X. Wang, W. Huang, S. Choudhury, Y. Zheng, C. V. Amanchukwu, S. T. Hung, Y. Ma, E. G. Lomeli, J. Qin, Y. Cui and Z. Bao, *Nat. Energy*, 2020, **5**, 526–533.

12 J. Qian, W. A. Henderson, W. Xu, P. Bhattacharya, M. Engelhard, O. Borodin and J.-G. Zhang, *Nat. Commun.*, 2015, **6**, 6362.

13 X. Cao, X. Ren, L. Zou, M. H. Engelhard, W. Huang, H. Wang, B. E. Matthews, H. Lee, C. Niu, B. W. Arey, Y. Cui, C. Wang, J. Xiao, J. Liu, W. Xu and J.-G. Zhang, *Nat. Energy*, 2019, **4**, 796–805.

14 Z. Zeng, V. Murugesan, K. S. Han, X. Jiang, Y. Cao, L. Xiao, X. Ai, H. Yang, J.-G. Zhang, M. L. Sushko and J. Liu, *Nat. Energy*, 2018, **3**, 674–681.

15 W. Xue, M. Huang, Y. Li, Y. G. Zhu, R. Gao, X. Xiao, W. Zhang, S. Li, G. Xu, Y. Yu, P. Li, J. Lopez, D. Yu, Y. Dong, W. Fan, Z. Shi, R. Xiong, C.-J. Sun, I. Hwang, W.-K. Lee, Y. Shao-Horn, J. A. Johnson and J. Li, *Nat. Energy*, 2021, **6**, 495–505.

16 X. Cao, L. Zou, B. E. Matthews, L. Zhang, X. He, X. Ren, M. H. Engelhard, S. D. Burton, P. Z. El-Khoury, H.-S. Lim, C. Niu, H. Lee, C. Wang, B. W. Arey, C. Wang, J. Xiao, J. Liu, W. Xu and J.-G. Zhang, *Energy Storage Mater.*, 2021, **34**, 76–84.

17 Z. Jiang, Z. Zeng, X. Liang, L. Yang, W. Hu, C. Zhang, Z. Han, J. Feng and J. Xie, Fluorobenzene, *Adv. Funct. Mater.*, 2021, **31**, 2005991.

18 X. Ren, L. Zou, X. Cao, M. H. Engelhard, W. Liu, S. D. Burton, H. Lee, C. Niu, B. E. Matthews, Z. Zhu, C. Wang, B. W. Arey, J. Xiao, J. Liu, J.-G. Zhang and W. Xu, *Joule*, 2019, **3**, 1662–1676.

19 Z. Jiang, Z. Zeng, W. Hu, Z. Han, S. Cheng and J. Xie, *Energy Storage Mater.*, 2021, **36**, 333–340.

20 D.-J. Yoo, S. Yang, K. J. Kim and J. W. Choi, *Angew. Chem., Int. Ed.*, 2020, **59**, 14869.

21 S. Chen, J. Zheng, L. Yu, X. Ren, M. H. Engelhard, C. Niu, H. Lee, W. Xu, J. Xiao, J. Liu and J.-G. Zhang, *Joule*, 2018, **2**, 1548–1558.

22 C. Niu, H. Lee, S. Chen, Q. Li, J. Du, W. Xu, J.-G. Zhang, M. S. Whittingham, J. Xiao and J. Liu, *Nat. Energy*, 2019, **4**, 551–559.

23 H. Zhang, Z. Zeng, F. Ma, X. Wang, Y. Wu, M. Liu, R. He, S. Cheng and J. Xie, *Adv. Funct. Mater.*, 2022, 2212000.

24 J. Zheng, G. Ji, X. Fan, J. Chen, Q. Li, H. Wang, Y. Yang, K. C. DeMella, S. R. Raghavan and C. Wang, *Adv. Energy Mater.*, 2019, **9**, 1803774.

25 S. Chen, J. Zheng, D. Mei, K. S. Han, M. H. Engelhard, W. Zhao, W. Xu, J. Liu and J.-G. Zhang, *Adv. Mater.*, 2018, **30**, 1706102.

26 X. Cao, P. Gao, X. Ren, L. Zou, M. H. Engelhard, B. E. Matthews, J. Hu, C. Niu, D. Liu, B. W. Arey, C. Wang, J. Xiao, J. Liu, W. Xu and J.-G. Zhang, *Proc. Natl. Acad. Sci. U. S. A.*, 2021, **118**, e2020357118.

27 J. Chen, X. Fan, Q. Li, H. Yang, M. R. Khoshi, Y. Xu, S. Hwang, L. Chen, X. Ji, C. Yang, H. He, C. Wang, E. Garfunkel, D. Su, O. Borodin and C. Wang, *Nat. Energy*, 2020, **5**, 386–397.

28 J. Chen, Q. Li, T. P. Pollard, X. Fan, O. Borodin and C. Wang, *Mater. Today*, 2020, **39**, 118–126.

29 C. V. Amanchukwu, X. Kong, J. Qin, Y. Cui and Z. Bao, *Adv. Energy Mater.*, 2019, **9**, 1902116.

30 J.-G. Zhang, W. Xu, J. Xiao, X. Cao and J. Liu, *Chem. Rev.*, 2020, **120**, 13312–13348.

31 T. D. Pham and K.-K. Lee, *Small*, 2021, **17**, 2100133.

32 T. D. Pham, A. Bin Faheem, J. Kim, H. M. Oh and K.-K. Lee, *Small*, 2022, **18**, 2107492.

33 Z. Yu, P. E. Rudnicki, Z. Zhang, Z. Huang, H. Celik, S. T. Oyakhire, Y. Chen, X. Kong, S. C. Kim, X. Xiao, H. Wang, Y. Zheng, G. A. Kamat, M. S. Kim, S. F. Bent, J. Qin, Y. Cui and Z. Bao, *Nat. Energy*, 2022, **7**, 94–106.

34 N. Yao, X. Chen, X. Shen, R. Zhang, Z.-H. Fu, X.-X. Ma, X.-Q. Zhang, B.-Q. Li and Q. Zhang, *Angew. Chem., Int. Ed.*, 2021, **60**, 21473.
35 X.-Q. Zhang, X.-B. Cheng, X. Chen, C. Yan and Q. Zhang, *Adv. Funct. Mater.*, 2017, **27**, 1605989.
36 H. Shi, J. Qin, K. Huang, P. Lu, C. Zhang, Y. Dong, M. Ye, Z. Liu and Z.-S. Wu, *Angew. Chem., Int. Ed.*, 2020, **59**, 12147–12153.
37 J. Wu, Z. Rao, X. Liu, Y. Shen, C. Fang, L. Yuan, Z. Li, W. Zhang, X. Xie and Y. Huang, *Adv. Mater.*, 2021, **33**, 2007428.
38 X. Fan, X. Ji, L. Chen, J. Chen, T. Deng, F. Han, J. Yue, N. Piao, R. Wang, X. Zhou, X. Xiao, L. Chen and C. Wang, *Nat. Energy*, 2019, **4**, 882–890.
39 X. Liu, X. Shen, H. Li, P. Li, L. Luo, H. Fan, X. Feng, W. Chen, X. Ai, H. Yang and Y. Cao, *Adv. Energy Mater.*, 2021, **11**, 2003905.
40 A. Nakanishi, K. Ueno, D. Watanabe, Y. Ugata, Y. Matsumae, J. Liu, M. L. Thomas, K. Dokko and M. Watanabe, *J. Phys. Chem. C*, 2019, **123**, 14229–14238.
41 S. Perez Beltran, X. Cao, J.-G. Zhang, P. Z. El-Khoury and P. B. Balbuena, *J. Mater. Chem. A*, 2021, **9**, 17459–17473.
42 M. Qin, M. Liu, Z. Zeng, Q. Wu, Y. Wu, H. Zhang, S. Lei, S. Cheng and J. Xie, *Adv. Energy Mater.*, 2022, 2201801.
43 H. Zhang, Z. Zeng, R. He, Y. Wu, W. Hu, S. Lei, M. Liu, S. Cheng and J. Xie, *Energy Storage Mater.*, 2022, 393–402.
44 H. J. S. Sand, *London, Edinburgh, Dublin Philos. Mag. J. Sci.*, 1901, 45–79.
45 Z. Wu, H. Liu, J. Holoubek, C. Anderson, L. Shi, H. Khemchandani, D. Lu, D. Liu, C. Niu, J. Xiao and P. Liu, *ACS Energy Lett.*, 2022, **7**, 2701–2710.
46 P. Bai, J. Li, F. R. Brushett and M. Z. Bazant, *Energy Environ. Sci.*, 2016, **9**, 3221–3229.
47 L. Reynolds, J. A. Gardecki, J. V. Frankland, M. L. Horng and M. Maroncelli, *J. Phys. Chem.*, 1996, **100**, 10337–10354.
48 Z. Yu, N. P. Balsara, O. Borodin, A. A. Gewirth, N. T. Hahn, E. J. Maginn, K. A. Persson, V. Srinivasan, M. F. Toney, K. Xu, K. R. Zavadil, L. A. Curtiss and L. Cheng, *ACS Energy Lett.*, 2022, **7**, 461–470.
49 N. Sun, R. Li, Y. Zhao, H. Zhang, J. Chen, J. Xu, Z. Li, X. Fan, X. Yao and Z. Peng, *Adv. Energy Mater.*, 2022, 2200621.
50 N. Piao, X. Ji, H. Xu, X. Fan, L. Chen, S. Liu, M. N. Garaga, S. G. Greenbaum, L. Wang, C. Wang and X. He, *Adv. Energy Mater*, 2020, **10**, 1903568.
51 Q.-K. Zhang, X.-Q. Zhang, L.-P. Hou, S.-Y. Sun, Y.-X. Zhan, J.-L. Liang, F.-S. Zhang, X.-N. Feng, B.-Q. Li and J.-Q. Huang, *Adv. Energy Mater*, 2022, **12**, 2200139.
52 D. Ruan, L. Tan, S. Chen, J. Fan, Q. Nian, L. Chen, Z. Wang and X. Ren, *ChemRxiv*, 2022, (preprint), DOI: **10.26434/chemrxiv-2022-kh1qq**.
53 L. Tan, S. Chen, Y. Chen, J. Fan, D. Ruan, Q. Nian, L. Chen, S. Jiao and X. Ren, *Angew. Chem., Int. Ed*, 2022, **61**, e202203693.
54 Y. Chen, Z. Yu, P. Rudnicki, H. Gong, Z. Huang, S. C. Kim, J.-C. Lai, X. Kong, J. Qin, Y. Cui and Z. Bao, *J. Am. Chem. Soc.*, 2021, **143**, 18703–18713.
55 T. Li, X.-Q. Zhang, N. Yao, Y.-X. Yao, L.-P. Hou, X. Chen, M.-Y. Zhou, J.-Q. Huang and Q. Zhang, *Angew. Chem., Int. Ed.*, 2021, **60**, 22683–22687.
56 Y. Zhang, Y. Wu, H. Li, J. Chen, D. Lei and C. Wang, *Nat. Commun.*, 2022, **13**, 1297.
57 W. Deng, W. Dai, X. Zhou, Q. Han, W. Fang, N. Dong, B. He and Z. Liu, *ACS Energy Lett.*, 2021, **6**, 115–123.
58 K. Huang, S. Bi, B. Kurt, C. Xu, L. Wu, Z. Li, G. Feng, X. Zhang and J. Gu, *Angew. Chem., Int. Ed.*, 2021, **60**, 19232–19240.
59 X.-Q. Zhang, T. Li, B.-Q. Li, R. Zhang, P. Shi, C. Yan, J.-Q. Huang and Q. Zhang, *Angew. Chem., Int. Ed.*, 2020, **59**, 3252–3257.
60 P. Zhao, Y. Li, S. Chen, H. Fan, Y. Feng, L. Hu, Y. Zhang, Q. Nie, H. Pei, C. Yang, J. Deng, C. Bao and J. Song, *Adv. Energy Mater*, 2022, **12**, 2200568.
61 Y.-H. Tan, G.-X. Lu, J.-H. Zheng, F. Zhou, M. Chen, T. Ma, L.-L. Lu, Y.-H. Song, Y. Guan, J. Wang, Z. Liang, W.-S. Xu, Y. Zhang, X. Tao and H.-B. Yao, *Adv. Mater.*, 2021, **33**, 2102134.
62 Z. Liu, D. Guo, W. Fan, F. Xu and X. Yao, *ACS Mater. Lett.*, 2022, **4**, 1516–1522.
63 X.-Q. Zhang, X. Chen, X.-B. Cheng, B.-Q. Li, X. Shen, C. Yan, J.-Q. Huang and Q. Zhang, *Angew. Chem., Int. Ed.*, 2018, **57**, 5301–5305.
64 C. Zhu, C. Sun, R. Li, S. Weng, L. Fan, X. Wang, L. Chen, M. Noked and X. Fan, *ACS Energy Lett.*, 2022, **7**, 1338–1347.
65 Y. Gao, M. Guo, K. Yuan, C. Shen, Z. Ren, K. Zhang, H. Zhao, F. Qiao, J. Gu, Y. Qi, K. Xie and B. Wei, *Adv. Energy Mater*, 2020, **10**, 1903362.
66 G. S. Mattei, Z. Li, A. A. Corrao, C. Niu, Y. Zhang, B. Liaw, C. C. Dickerson, J. Xiao, E. J. Dufek and P. G. Khalifah, *Chem. Mater.*, 2021, **33**, 2378–2386.
67 C. Niu, D. Liu, J. A. Lochala, C. S. Anderson, X. Cao, M. E. Gross, W. Xu, J.-G. Zhang, M. S. Whittingham, J. Xiao and J. Liu, *Nat. Energy*, 2021, **6**, 723–732.